Atmos. Meas. Tech., 5, 487–500, 2012
www.atmos-meas-tech.net/5/487/2012/
doi:10.5194/amt-5-487-2012

Atmospheric Measurement Techniques

HCl and ClO in activated Arctic air; first retrieved vertical profiles from TELIS submillimetre limb spectra

A. de Lange[1], M. Birk[2], G. de Lange[1], F. Friedl-Vallon[4], O. Kiselev[3], V. Koshelets[3], G. Maucher[4], H. Oelhaf[4], A. Selig[1], P. Vogt[2], G. Wagner[2], and J. Landgraf[1]

[1]SRON – Netherlands Institute for Space Research, Utrecht, The Netherlands
[2]Deutsches Zentrum für Luft und Raumfahrt, Institut für Methodik der Fernerkundung, Wessling, Germany
[3]The Kotel'nikov Institute of Radio Engineering and Electronics, Russian Academy of Science, Moscow, Russia
[4]Karlsruhe Institute of Technology, Institute for Meteorology and Climate Research, Karlsruhe, Germany

Correspondence to: A. de Lange (a.de.lange@sron.nl)

Received: 10 October 2011 – Published in Atmos. Meas. Tech. Discuss.: 25 October 2011
Revised: 12 January 2012 – Accepted: 13 January 2012 – Published: 28 February 2012

Abstract. The first profile retrieval results of the Terahertz and submillimeter Limb Sounder (TELIS) balloon instrument are presented. The spectra are recorded during a 13-h balloon flight on 24 January 2010 from Kiruna, Sweden. The TELIS instrument was mounted on the MIPAS-B2 gondola and shared this platform with the Michelson Interferometer for Passive Atmospheric Sounding (MIPAS) and the mini-Differential Optical Absorption Spectroscopy (mini-DOAS) instruments. The flight took place within the Arctic vortex at an altitude of ≈34 km in chlorine activated air, and both active (ClO) and inactive chlorine (HCl) were measured over an altitude range of respectively ≈16–32 km and ≈10–32 km. In this altitude range, the increase of ClO concentration levels during sunrise has been recorded with a temporal resolution of one minute. During the daytime equilibrium, a maximum ClO level of 2.1 ± 0.3 ppbv has been observed at an altitude of 23.5 km. This equilibrium profile is validated against the ClO profile by the satellite instrument Microwave Limb Sounder (MLS) aboard EOS Aura. HCl profiles have been determined from two different isotopes – $H^{35}Cl$ and $H^{37}Cl$ – and are also validated against MLS. The precision of all profiles is well below 0.01 ppbv and the overall accuracy is therefore governed by systematic effects. The total uncertainty of these effects is estimated to be maximal 0.3 ppbv for ClO around its peak value at 23.5 km during the daytime equilibrium, and for HCl it ranges from 0.05 to 0.4 ppbv, depending on altitude. In both cases the main uncertainty stems from a largely unknown non-linear response in the detector.

1 Introduction

After the "Montreal Protocol on Substances that Deplete the Ozone Layer" went into effect, anthropogenic chlorofluorocarbons (CFCs) emissions started being phased out. Although the stratospheric HCl content has been declining since 1997 (Jones et al., 2011), the rate of the decline of the total atmospheric chlorine content and subsequently the rate of the expected recovery of ozone abundances varies among different simulations of atmospheric chemistry models (see e.g. Austin et al., 2010 and references therein). Therefore, monitoring stratospheric chlorine species is still important for our understanding of their impact on stratospheric ozone.

The partitioning between active and inactive chlorine dictates the relative strength of the chlorine ozone-loss cycle (see e.g. Solomon, 1999). During the polar winter, inactive or reservoir chlorine is converted into active chlorine in the polar vortex, increasing the strength of this loss cycle. To estimate the total stratospheric chlorine content, both reservoir and active chlorine species need to be known. The main chlorine reservoir species is hydrogen chloride (HCl), whereas the foremost active molecular chlorine compound at daytime is chlorine monoxide (ClO).

At nighttime, ClO is converted into $ClONO_2$ and the ClO-dimer, depending on the relative abundances of NO_2 and ClO. In the activated polar vortex, not only ClO abundances are high but NO_2 concentration levels are low as well because of a steady conversion into N_2O_5 and subsequently into HNO_3, favouring the formation of the ClO-dimer during sunset. During sunrise these species are back-converted

into ClO by photo-dissociation processes, leading to a diurnal cycle of ClO concentrations.

In 2007, new laboratory photo-dissociation rates of the ClO-dimer were presented by Pope et al. (2007). These rates led to an underestimation of modeled ClO levels with respect to observations when implemented in chemical models (von Hobe et al., 2007). Several studies have since then indicated that the measurements by Pope et al. (2007) may be faulty (von Hobe et al., 2009; Lien et al., 2009; Papanastasiou et al., 2009; Jin et al., 2010; Wetzel et al., 2010). The formation rate of ClO during sunrise is, especially in the polar vortex, strongly linked with the photo-dissociation rates of the ClO-dimer.

Global coverage of stratospheric profiles for both HCl and ClO have been available since 1991 by satellite instruments. In that year the UARS satellite was launched with the Halogen Occultation Experiment (HALOE) (Russell et al., 1993) aboard, probing HCl, and the Microwave Limb Sounder (MLS) (Barath et al., 1993) that observed ClO. This satellite was operational until 2005 and had therefore overlap with the next generation of satellite instruments: Sub-Millimeter Receiver (SMR) (Frisk et al., 2003) aboard Odin, Michelson Interferometer for Passive Atmospheric Sounding (MIPAS) (Glatthor et al., 2004) on Envisat, Atmospheric Chemistry Experiment (ACE) (Bernath et al., 2005) aboard SCISAT-1 and a new and updated MLS (Waters et al., 2006) on EOS-Aura. The SMR started its measurements in 2001, MIPAS in 2002, and both ACE and MLS in 2004. All four instruments are still operational. MIPAS and SMR record ClO whereas ACE measures HCl. The updated MLS observes both HCl and ClO. In 2009, the Superconducting Submillimeter-Wave Limb-Emission Sounder (SMILES) (Kikuchi et al., 2010) was installed on the International Space Station and has been recording HCl and ClO spectra until 2010.

In addition to satellite measurements, several balloon instruments that record HCl and ClO were also operational in the past two decades, partly as satellite validation platforms, but also to conduct science. HCl profiles have, for instance, been measured in the early 90s by the ALIAS aircraft instrument and the balloon instruments BLISS and MkIV (Webster et al., 1994) and later by the balloon instruments SPIRALE (Moreau et al., 2005) and B-SMILES (Irimajiri et al., 2006). The latter was a pre-cursor of the SMILES space instrument and has observed ClO as well. The MIPAS balloon instrument (Friedl-Vallon et al., 2004) has observed ClO during all flights in the Arctic over the last 20 years (e.g. Wetzel et al., 2010).

On 24 January 2010, the Terahertz and submillimeter Limb Sounder (TELIS) (Birk et al., 2010) was launched around midnight from Kiruna, North Sweden. The instrument was mounted on the MIPAS-B2 gondola together with MIPAS (Friedl-Vallon et al., 2004) and the mini-Differential Optical Absorption Spectroscopy (mini-DOAS) (Weidner et al., 2005) instruments. The flight duration was 13 h and occurred in the Arctic polar vortex at an altitude of ≈34 km. At that time the vortex was fully chlorine activated, leading to the complete absence of HCl around 23 km and a peak in the ClO concentration of ≈2 ppbv at this altitude.

TELIS is a cryogenic instrument and the noise levels are therefore very low, allowing for precise measurements of many species. The instrument is capable of detecting the chlorine species HCl, ClO, and HOCl. In combination with MIPAS (ClO, $ClONO_2$, and the ClO-dimer) and mini-DOAS (OClO), both probing the same air masses as TELIS, an extensive set of chlorine species is available, which is very suitable for constraining the total stratospheric chlorine content.

Unique about TELIS is that it monitors the ClO diurnal variation with a temporal resolution of ≈1 min. This, together with the MIPAS observations of the nighttime reservoir species $ClONO_2$ and the ClO-dimer, allows for testing ClO formation rates as function of altitude, and thus as function of temperature and pressure, in atmospheric chemistry models. As this formation rate is directly linked to the ClO-dimer photo-dissociation rate in the chlorine activated polar vortex, the joint MIPAS-TELIS balloon flight of 2010 makes it very suitable to evaluate the dissociation rates found in laboratory experiments.

In this paper we present ClO and HCl profile retrievals from the 24 January 2010 TELIS flight, including a comparison with co-located MLS measurements and an extensive error analysis. The outline of the present study is as follows: in Sect. 2 the TELIS instrument and measurements are described. Background information on the inversion method used in this study, is given in Sect. 3. Subsequently, the first profile retrieval results for both HCl and ClO are presented and discussed in Sect. 4. In this section, the error budget for the profiles is discussed as well as the validation of the retrieval results. Finally, Sect. 5 concludes the study.

2 TELIS

2.1 Instrument

TELIS is a cryogenic heterodyne balloon sounder developed in a collaboration of three institutes: the leading institute German Aerospace Center (DLR), Germany, Rutherford Appleton Laboratory (RAL), United Kingdom, and Netherlands Institute for Space Research (SRON), the Netherlands. Each institute is responsible for one channel: a miniaturised 500 GHz channel (RAL), a tunable 1.8 THz channel (DLR), and a tunable 480–650 GHz channel (SRON). The results presented here pertain to the 480–650 GHz channel developed by SRON in collaboration with the Institute of Radio-Engineering and Electronics (IREE), Moscow. The key-technology of this channel is the development of a tunable superconducting integrated receiver (SIR). This $4 \times 4\,mm^2$ receiver combines a tremendous miniaturisation over traditional electronic circuits, with almost no loss in noise properties. The double sideband system noise temperature is 250 K,

which is indeed very comparable to the cryogenic spaceborne ISS/SMILES instrument that has a single sideband noise temperature of 330 K (Ochiai et al., 2010), being equivalent to a double sideband noise temperature of 230 K. A detailed description of the SIR channel is given by de Lange et al. (2010). The most important instrument characteristics, including an uncertainty estimate, are described below. The uncertainties are also summarised in Table 1.

The TELIS back-end consists of a digital autocorrelator spectrometer (DACS) and yields the digitised autocorrelation of the measured signal as raw data, or level-0 data product. This data is post-processed on ground to a level-1 data product, which is used as input for the retrievals. The level-1 data product consists of radiometric calibrated limb spectra and their geo-location and pointing angles as well as the sideband ratio information and the antenna beam profile of the instrument.

The following post-processing steps are taken to obtain the level-1-product: A 3-level digital autocorrelator is used as a spectrometer. To cover the instrument bandwidth of 2 GHz, the IF-signal is split into four 500 MHz segments which are complex sampled. For each frequency segment the true autocorrelation is estimated from the measured, digitised autocorrelation using a quantisation correction approach (Kulkarni and Heiles, 1980). The true autocorrelation function is Fourier transformed to obtain the power spectra. An apodisation function is applied and is taken into account in the instrumental line shape of the instrument. The spectral resolution is 2.2 MHz and, as the narrowest atmospheric lines in the SIR recordings have a full width half-maximum (FWHM) of ≈10 MHz, all lines are well sampled with at least 4 points.

During flight a short term, linear calibration approach is employed. An on-board black body unit is used as a hot signal reference and the signal from pointing into deep space is used as a cold signal reference. The uncertainty in the temperature of the black body is estimated to be 1 K.

From these hot and cold calibration measurements, the unknowns of the instrument's response function, the radiometric gain and the offset, can be determined and thus allow for a linear radiometric calibration of the processed limb spectra.

With the heterodyne measurement technique, a reference signal with fixed frequency is generated on-board in the so-called local oscillator (LO). This signal is mixed with the atmospheric signal in a non-linear mixer, resulting in signals with sum and difference frequencies of the LO and atmospheric signal. Only the signal with the difference frequency is processed; all other signals are filtered out. The atmospheric signal can be reconstructed from this signal if the characteristics of the LO are known. For the SIR channel, the LO frequency ν_{LO} ranges from 480 GHz to 650 GHz and is known within 1 MHz. In Table 1, the instrumental line shape (ILS) spectral ratio refers to the fraction of LO power stored in a central delta-function-like peak (much narrower than 1 spectral bin of the detector), as opposed to the power stored in sidelobes ≈10 MHz away from the central frequency. This number determines the overall ILS spectrum for the SIR channel. The accuracy of this ratio is better than 10 % and determines mostly the ILS error spectrum.

Table 1. Uncertainties in instrumental parameters used to determine the error budget for the HCl and ClO profile retrievals from the SIR channel of the TELIS instrument. ILS stands for instrumental line shape and LO for local oscillator.

Error source	Uncertainty
Field of view width	1 %
ILS spectral ratio	10 %
LO frequency	1 MHz
Sideband ratio	5 %
Calibration black body	1 K
Pointing	1 arcmin
Non-linearity	10–25 % (see text)

In case of the SIR channel, the signal is recorded as function of the absolute difference frequency, or intermediate frequency (IF). This means that the recorded spectrum is the superposition of two spectral bands: $\nu_{LO} + \nu_{IF}$ and $\nu_{LO} - \nu_{IF}$, with ν_{LO} the LO frequency and ν_{IF} = 5–7 GHz the IF frequency band. In the ideal case, the recorded signal has the same sensitivity to both spectral bands. The relative sensitivity to these two bands, the so-called sideband ratio, is thus preferably around one. For the SIR channel this ratio is between 0.6 and 1.4 and is known within 5 % for every local oscillator frequency relevant during flight.

A limb sequence consists of sequential observations with different viewing geometries such that the instrument line of sights observe the atmosphere within a given altitude range, which is indicated by their tangent heights. For HCl, the limb sequence covered tangent heights from 10–32.5 km in steps of 1.5 km, complemented with two up-looking observations at respectively 6° and 12° to assess the atmosphere above the balloon. For ClO, the limb sequence started at 16 km, but besides this its assessment process identical to that of HCl. Both limb sequences covered the altitude range of chlorine activated air (17–26 km).

The tangent heights in this study refer to the commanded tangent heights, but the actual heights probed by the SIR channel are slightly lower due to an off-centre optical alignment, and are accounted for in the retrievals. The systematic offset is −6 arcmin for HCl and −4.5 arcmin for ClO. These angles correspond to a maximal altitude offset of ≈970 m for HCl at its lowest tangent height (10 km) and ≈630 m for ClO (16 km). The uncertainty in the absolute pointing offset is estimated to be 1 arcmin, corresponding to ≈150 m for the lowest tangent heights. It is noted that atmospheric refraction lowers the tangent heights further, and this is also taken into account in the retrievals.

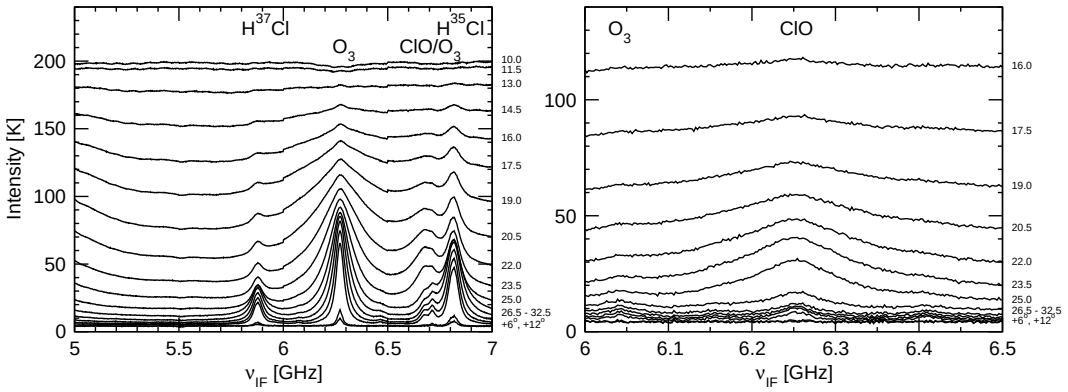

Fig. 1. SIR TELIS measurements of atmospheric HCl and ClO. In the left panel the average of 10 limb sequences, covering HCl lines of both isotopes, is depicted as function of the intermediate frequency ν_{IF}. The local oscillator frequency is $\nu_{LO} = 619.1$ GHz. In the right panel a single limb scan is given for the dedicated ClO micro-window at daytime equilibrium, with $\nu_{LO} = 507.52$ GHz. The corresponding tangent heights for each limb sequence are given in km to the right of the particular panel.

The pointing uncertainty is derived as follows: The MIPAS instrument on the balloon gondola is equipped with a dedicated attitude and heading reference system with a stability much better than 1 arcmin (Friedl-Vallon et al., 2004). Although TELIS receives the information from this system as well, MIPAS and TELIS are both connected to the gondola frame by several springs that may not only introduce an additional pointing offset, but also deteriorate the pointing stability. From the reproducibility of subsequent spectra, however, it can be determined that the pointing stability for the TELIS instrument is much better than 1 arcmin. On ground, with the gondola suspended in air and with all instruments in place, the pointing offset of the SIR channel has been determined with an absolute accuracy of ≈1 arcmin. It is this accuracy that is taken as the uncertainty of the pointing error. During flight, O_2 and O_3 measurements are performed to provide additional information on the exact pointing. In the future, these measurements will be incorporated in the data analysis.

The geo-location information is also taken from the MIPAS attitude and heading reference system.

The antenna beam profile, or field of view, of the SIR channel is almost Gaussian shaped with a full width half-maximum (FWHM) in the vertical direction of ≈12 arcmin at 495 GHz (Birk and Wagner, 2009) and is known within 1 %. This translates to ≈1.5 km at a tangent point of 26 km. The steps in the limb sequence are set to this vertical resolution of 1.5 km to resolve the vertical distribution of ClO and HCl. The field of view in the horizontal direction is twice as large, but horizontal gradients in the atmosphere are much smaller than vertical gradients and may be neglected on this scale.

In a previous study for the SIR channel on rare water isotopes, it has been shown that especially the sideband ratio and the pointing error are critical instrument parameters for profile retrieval and should be known accurately (de Lange et al., 2009). With the actual instrument becoming ready, another critical instrument parameter became apparent, being the non-linearity in the detector's response function. These parameters have been determined during dedicated on-ground calibration campaigns (Birk et al., 2010), albeit that the non-linearity still shows a large uncertainty.

The effect of non-linearity is a signal compression with respect to a linear response, as function of total input power. In case of the TELIS SIR channel, this is mainly caused by the saturation of two different amplifiers of which one is deeply embedded in the spectrometer. Compression levels of 10–25 % are found for the measurements with the highest total powers.

2.2 Measurements

Only two HCl lines occur within the 480–650 GHz frequency range of the TELIS SIR channel[1], one for each Cl isotope: $H^{37}Cl$ has a transition at 625.0 GHz and $H^{35}Cl$ at 625.9 GHz. With the local oscillator frequency $\nu_{LO} = 619.1$ GHz, both lines fall within the $\nu_{IF} = 5$–7 GHz frequency range of the SIR channel. TELIS measurements in this spectral range are depicted in the left panel of Fig. 1. The two HCl lines are clearly visible around $\nu_{IF} = 5.9$ GHz and $\nu_{IF} = 6.8$ GHz, respectively. In the wing of the latter line, a ClO feature is discernible. However, this feature is relatively weak and for lower tangent heights the HCl line dwarfs the ClO line due to pressure broadening. Therefore, for the retrieval of ClO, a dedicated measurement window has been defined with a local oscillator frequency of $\nu_{LO} = 507.52$ GHz, probing the isolated ClO line at 501.27 GHz. The signals from this line are so strong, especially in chlorine activated air, that a single limb sequence is sufficient for profile retrieval, allowing for

[1]Because of hyperfine splitting, each line is in fact a triplet of overlapping lines.

monitoring changes in ClO levels over time with a temporal resolution of 1 min, being the duration of one limb sequence including calibration measurements. The increase of ClO concentrations from nighttime to daytime levels have been monitored for 1.5 h during sunrise. The right panel of Fig. 1 shows a single limb sequence when the ClO concentrations have reached their daytime equilibrium.

3 Inversion

For the interpretation of the TELIS measurements, a forward model $\boldsymbol{F}$ is needed that simulates the radiance measurement $\boldsymbol{r}$ as function of the atmospheric state vector $\boldsymbol{x}$ and the forward model parameter vector $\boldsymbol{b}$,

$$\boldsymbol{r} = \boldsymbol{F}(\boldsymbol{x}, \boldsymbol{b}) + \boldsymbol{e}_y, \quad (1)$$

where $\boldsymbol{e}_y$ comprises forward model error and instrument error including the measurement noise. The state vector $\boldsymbol{x}$ contains all parameters to be retrieved from the measurement. Depending on the particular retrieval, it contains the HCl or the ClO profile and atmospheric abundance profiles of interfering species. The forward model parameter $\boldsymbol{b}$ summarises all model parameters that have to be known a priori, like instrument parameters or atmospheric pressure and temperature profiles.

The forward model comprises the solution of the radiative transfer equation in a non-scatering atmosphere for thermal equilibrium in spherical geometry, resulting in the intensity as function of frequency, at the gondola altitude in the viewing direction of the instrument. It is a line by line model and only lines from the HITRAN 2008 database (Rothman et al., 2009) are included that have a contribution of more than 0.001 K to the limb spectrum with a tangent height of 25 km in standard atmosphere. To account for broadband continuum emissions, the Liebe 1993 continuum model (Liebe et al., 1993) has been adopted. Refraction of the limb path is accounted for by implementing a non-dispersive refractive index, as is described by Buehler et al. (2005). The forward model also includes an instrument model to account for the specifics of the TELIS instrument. For more details on the forward model we refer to de Lange et al. (2009).

To determine the atmospheric state vector $\boldsymbol{x}$ from Eq. (1) the forward model $\boldsymbol{F}$ has to be inverted. In general forward model $\boldsymbol{F}$ is not linear in the state vector $\boldsymbol{x}$, and so Eq. (1) is inverted with a Gauss-Newton iteration scheme. For this purpose $\boldsymbol{F}$ is linearised in iteration step i by a Taylor expansion around the solution of the previous iteration step, $\boldsymbol{x}_{i-1}$, starting with a first guess state vector $\boldsymbol{x}_0$. Thus, Eq. (1) can be rewritten as

$$\boldsymbol{y} = \mathbf{K}\,\boldsymbol{x} + \boldsymbol{e}_y, \quad (2)$$

where $\boldsymbol{y} = \boldsymbol{r} - \boldsymbol{F}(\boldsymbol{x}_{i-1}) + \mathbf{K}\boldsymbol{x}_{i-1}$ is the so-called measurement vector and $\mathbf{K}$ is the Jacobian matrix.

For limb measurements each recorded spectrum probes predominately the atmospheric state at its tangent height, and therefore all spectra of a limb scan contain different information about the probed vertical range of the atmosphere. At first glance, one may think that the atmospheric trace gas profiles can be retrieved uniquely within this altitude range at vertically homogeneous layers defined by the vertical scan of the atmosphere. However, the atmosphere above the instrument, which is not properly observed by TELIS, may not be neglected in the forward model and thus in the retrieval. Also, below the lowest tangent point the atmosphere is probed because of the extended field of view of the instrument. Thus, the inversion of vertical HCl and ClO profiles represents an ill-posed problem which means that the standard least squares solution is overwhelmed by noise. Several techniques have been developed to tackle this problem and in this study we employ Tikhonov regularisation (Tikhonov, 1963; Phillips, 1962; Twomey, 1963). This inversion technique is used frequently for the interpretation of atmospheric limb measurements (e.g. Schimpf and Schreier, 1997; Steck, 2002; Wetzel et al., 2010). The corresponding minimisation function becomes

$$\boldsymbol{x}_\gamma = \min_x \left(\|\mathbf{S}_y^{-\frac{1}{2}} (\mathbf{K}\,\boldsymbol{x} - \boldsymbol{y})\|^2 + \gamma^2 \|\mathbf{L}\,\boldsymbol{x}\|^2 \right), \quad (3)$$

where $\boldsymbol{x}_\gamma$ is the solution vector of the minimisation problem, $\|\mathbf{S}_y^{-\frac{1}{2}}(\mathbf{K}\boldsymbol{x} - \boldsymbol{y})\|^2$ is the least squares norm with $\mathbf{S}_y$ the measurement noise covariance matrix, and $\|\mathbf{L}\boldsymbol{x}\|^2$ is the side constraint in which $\mathbf{L}$ is a suitably chosen matrix. In this study the first derivative of the state vector $\boldsymbol{x}$ is used as a side constraint and $\mathbf{L}$ is the matrix representation of this first derivative. γ is the regularisation parameter, balancing the contributions of the least square term and the side constraint. The corresponding cost function in Eq. (3) is transformed to the standard form with $\mathbf{L} = \mathbf{I}$, the unity matrix, as described by Eldén (1977).

The value of γ is of crucial importance for the retrieval. If γ is chosen too large, the noise contribution to the solution of the measurement is low, but the least squares residual norm deviates significantly from its minimum, indicating that the calculated spectrum corresponding to this solution deviates from the actual measurement. On the other hand, if γ is chosen too small, the measurement is fitted well but the solution norm is high, and so, the solution is overwhelmed by noise. The part of the profile that is dominated by noise defines the effective null-space of the problem. Thus, γ should be chosen such that the two minimizations are well balanced.

To find the appropriate value for the regularisation parameter, the L-curve is used (Hansen, 1992). This curve is a parametric plot of the logarithm of the solution norm $\|\boldsymbol{x}_\gamma\|^2$ and the logarithm of the least squares norm $\|\mathbf{S}_y^{-\frac{1}{2}}(\mathbf{K}\boldsymbol{x}_\gamma - \boldsymbol{y})\|^2$ as function of regularisation parameter γ. The curve is generally L-shaped and the regularisation parameter that corresponds to the corner balances the two terms in the cost

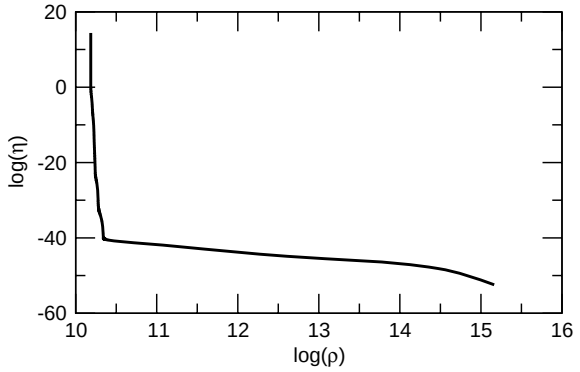

Fig. 2. An example of the L-curve used in this study. This particular curve pertains to the last ClO measurement after the transformation of the cost function into standard form. In this figure η refers to the norm of the transformed state vector and ρ to the norm of the transformed least squares term. The regularisation parameter corresponding to the lower left corner is used to determine the retrieved state vector.

function as described in Eq. (3). An example of such a curve is given in Fig. 2. This results in a stable state vector $\boldsymbol{x}_\gamma$ that represents the measurement and, at the same time, is as much as possible determined by the atmospheric condition as opposed to measurement noise. The solution is then

$$\boldsymbol{x}_\gamma = \mathbf{D}\,\boldsymbol{y}, \tag{4}$$

where

$$\mathbf{D} = \left(\mathbf{K}^T\,\mathbf{S}_y^{-1}\,\mathbf{K} + \gamma^2\,\mathbf{L}^T\,\mathbf{L}\right)^{-1}\mathbf{K}^T\,\mathbf{S}_y^{-1}, \tag{5}$$

is the pseudo-inverse of $\mathbf{K}$ or the contribution matrix.

The measurement noise is propagated into the retrieved state vector as

$$\mathbf{S}_x = \mathbf{D}\,\mathbf{S}_y\,\mathbf{D}^T, \tag{6}$$

where $\mathbf{S}_x$ is the retrieval noise covariance matrix.

The retrieved vector $\boldsymbol{x}_\gamma$ is a weighted average of the true atmospheric state vector $\boldsymbol{x}_{\text{true}}$

$$\boldsymbol{x}_\gamma = \mathbf{A}\,\boldsymbol{x}_{\text{true}} + \boldsymbol{e}_x, \tag{7}$$

where $\mathbf{A} = \mathbf{DK}$ is the averaging kernel and $\boldsymbol{e}_x = \mathbf{D}\boldsymbol{e}_y$ the error in the state vector caused by measurement errors. Effectively, the averaging kernel filters out the null-space contribution of the true state vector $\boldsymbol{x}_{\text{true}}$. When the kernel is peaked at the tangent height of the limb observation, it can be interpreted as a smoothing function and its width can viewed upon as the vertical resolution of the retrieved profile.

To estimate the effect of measurement errors $\mathrm{d}\boldsymbol{y}$ due to uncertainties of both the instrument calibration and a priori knowledge on the atmospheric state in the linear approximation, we apply

$$\mathrm{d}\boldsymbol{x} = \mathbf{D}\,\mathrm{d}\boldsymbol{y}, \tag{8}$$

Table 2. Overview of the retrieved parameters for each retrieval.

Retrieval	HCl	ClO	offset	O_3
$H^{35}Cl$	✓	✓	✓	✓
$H^{37}Cl$	✓	–	✓	✓
ClO	–	✓	✓	–

where $\mathrm{d}\boldsymbol{x}$ is the contribution to the error budget of the retrieved state vector. In the presented study the contributions to the error budget have been determined using Eq. (8), except for the non-linear detector response function for which a full retrieval was performed. The non-linearity is the largest error source and in this case the linear approximation is not valid.

4 Retrievals

In this section we analyse the retrieval of HCl and ClO profiles from TELIS SIR measurements. For each retrieval a spectral window of 500 MHz, corresponding to a single spectrometer segment, is considered. The HCl retrievals are performed separately for both chlorine isotopes. The state vector $\boldsymbol{x}$ contains the HCl and ClO profiles, respectively, discretised vertically in 1.5 km thick homogeneous layers, over an altitude range of 8.5–64 km for HCl and 14.5–64 km for ClO.

In addition, the state vector includes a radiometric offset for each spectrum in the limb sequence. The offsets are of most importance for the lower tangent heights where broad continuum contributions to the spectra are not accurately represented by the atmospheric forward model. Furthermore, in case of HCl the state vector includes atmospheric abundance profiles of species that interfere with the HCl emission lines in both spectral bands. The state vector set up for the different retrievals is summarised in Table 2.

Between the two HCl lines a strong ozone line occurs, as can be seen in the panel on the left in Fig. 1. This line broadens towards lower tangent heights and induces a sloped background for both HCl lines. To account for this background, an ozone profile was retrieved simultaneously with the HCl profiles. In case of $H^{35}Cl$, also a weak ClO feature occurs in the wing of the line. To account for this, a ClO profile was retrieved in addition. The ozone and ClO profiles are not meant to be data products, but are merely included to improve the fit and the HCl data product.

The TELIS retrieval requires a priori knowledge on several parameters, which are summarized by the forward model parameter vector $\boldsymbol{b}$. It contains the instrument characteristics of Table 1, which have been determined in separate on-ground measurement campaigns. As mentioned in Sect. 2.1, the non-linearity in the detector causes a compression of 10–25 % in the hot calibration measurements. This range can

Table 3. Uncertainties in spectroscopic and atmospheric parameters used to determine the error budget for the HCl and ClO profile retrievals from the SIR channel of the TELIS instrument.

Error source	Uncertainty
Line strength	2 % (HCl)
	5 % (ClO)
Air broadening	5 %
Temperature profile	1 K
Pressure profile	1 %

be rewritten as $17.5\,\% \pm 7.5\,\%$. In the retrievals, the central value of 17.5 % compression is used. To assess the error propagation on the retrieval products, the retrievals are repeated with the compression set to 10 % and 25 % respectively, and the error is taken as the difference profile of 17.5 % and 10 %, which is almost equal to the difference between the profiles of 17.5 % and 25 %.

Furthermore, the forward model parameter vector $\boldsymbol{b}$ contains vertical profiles of water vapour, N_2O, and, in case of ClO retrieval, ozone that have been taken from the MLS data centre (http://mirador.gsfc.nasa.gov/). The temperature and pressure profiles are taken from the retrievals of the MIPAS instrument, with whom TELIS shares the gondola (G. Wetzel, personal communication, 2011). Both instruments have almost identical viewing geometries, and the same air masses are probed. The error on the temperature profile is 0.5–1 K (Wetzel et al., 2002) and in this study the upper limit of 1 K is taken. This error captures all temperature dependencies, including atmospheric black-body radiation, partition function of quantum level population, and the temperature dependence of the spectroscopic broadening coefficient. The error on the pressure profile is estimated to be 1 %. The profiles of remaining trace gases are only of minor importance and are fixed to the standard AFGL US winter atmosphere (Anderson et al., 1986). The spectroscopic parameters, needed in the forward model, are taken from the HITRAN 2008 spectroscopic database (Rothman et al., 2009). The uncertainties in the spectroscopic widths (5 %) and line strengths (5 % for ClO and 2 % for HCl) are also taken from this database. For completeness, the spectroscopic and atmospheric uncertainties used in this study to estimate their effect on the retrieved profiles are listed in Table 3.

For validation, MLS HCl and ClO profiles are taken. These profiles were recorded at ≈200 km distance of the balloon and care is taken that each pertained to chlorine activated stratospheric air. The time difference of the MLS and TELIS measurements was ≈1.5 h for HCl and ≈2.5 h for the ClO measurement during daytime equilibrium. Also the MLS ClO recording was taken under daytime equilibrium conditions.

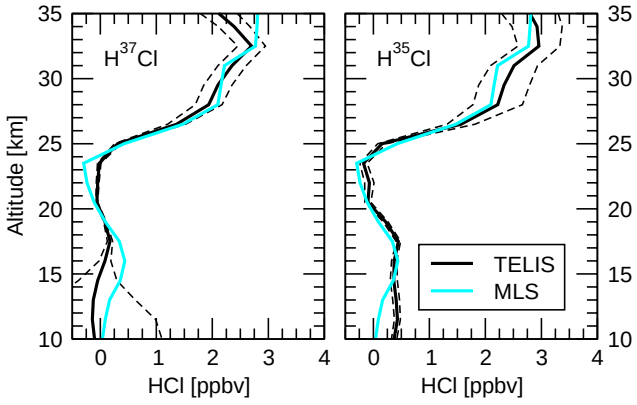

Fig. 3. The retrieved HCl vertical profiles in ppbv from the TELIS balloon flight on 24 January 2010 in chlorine activated Arctic air. The minimum in the profiles around 23 km is due to the conversion of inactive reservoir chlorine into active chlorine. The left panels pertain to $H^{37}Cl$ and the right to $H^{35}Cl$. The profiles are shown in black for TELIS and in blue for the MLS instrument. The dashed lines indicate the overall accuracy in the TELIS profiles.

4.1 HCl retrieval

In this section the HCl retrieval results, including the error budget, are discussed, where the following definitions are used: with precision, the error propagation of measurement noise onto the retrieved profile is meant. The term systematic error refers to systematic effects in the retrieved profiles due to uncertainties in instrument and atmospheric parameters.

HCl profiles have been retrieved from TELIS spectra. The spectra are an average of 10 subsequent limb sequences. This is valid as HCl concentrations do not vary during the measurements. Although the measurement error is not dominated by the random noise on the measurement, systematic errors with pseudo-noise characteristics average out in the mean. The retrieved HCl profiles are depicted in Fig. 3 for both chlorine isotopes (solid black lines). It is noted that the natural abundances for the isotopes have been accounted for and that the concentrations refer to total HCl amounts. The profile determined from $H^{37}Cl$ is plotted in the left panel and from $H^{35}Cl$ in the right panel. The balloon flight took place in activated air, which can clearly be seen in Fig. 3 by the absence of HCl around 23 km – all of the HCl has been converted into active chlorine species, such as ClO. Because of the very low noise on the spectra the precision of the profiles are below 0.01 ppbv and are not discernible on this scale. The overall accuracy in the profiles is not determined by measurement noise, but by systematic effects induced by uncertainties in the knowledge of instrument and atmospheric parameters. This total accuracy is indicated with dashed lines. The MLS HCl profile is depicted in blue for reference.

The averaging kernels are shown in Fig. 4 for $H^{37}Cl$ (left panel) and $H^{35}Cl$ (centre panel). The corresponding FWHM of the kernels are plotted in the panel on the right-hand

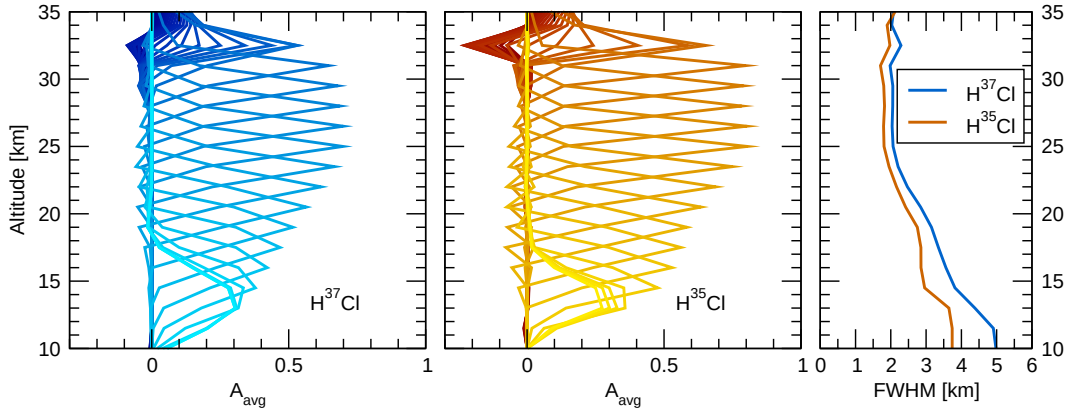

Fig. 4. Averaging kernels for $H^{37}Cl$ (left panel) and $H^{35}Cl$ (centre) with the FWHM of the kernels in respectively blue and red (right panel).

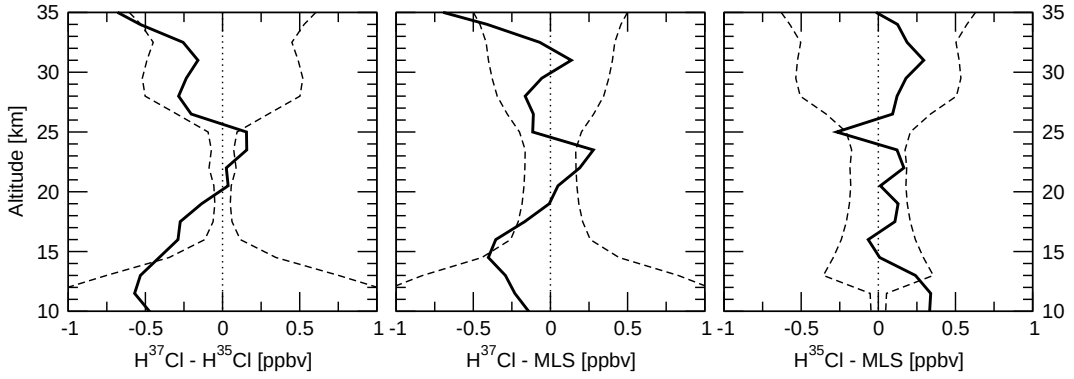

Fig. 5. The differences between the two TELIS HCl profiles, the TELIS $H^{37}Cl$ and MLS profiles, and the TELIS $H^{35}Cl$ and MLS profiles are plotted in respectively the left, central, and right panel. The dashed lines indicate the RSS of the precision and all systematic errors of both particular profiles.

side. For both isotopes the kernels are peaked in the altitude range 15–32.5 km and the widths may be interpreted as a measure of the vertical spatial resolution. Above 25 km the FWHM = 2 km ($H^{37}Cl$) and 1.8 km ($H^{35}Cl$) which is close to the values of the instrumental field of view (1.5 km) and the steps between two consecutive tangent heights (also 1.5 km). Below 15 km, the kernels continuously broaden to widths of 3.7 km ($H^{37}Cl$) and 2.9 km ($H^{35}Cl$) due to the fact that the spectra become saturated at low altitudes and no HCl features are any longer discernible (see also Fig. 1). Below 15 km, the peak of the averaging kernel does not correspond to the tangent height, which indicates only very little height sensitivity of the retrieval in this altitude range.

In Fig. 5 the difference between the two TELIS profiles is depicted in the left panel. The differences between the TELIS and MLS profiles are shown in the central panel ($H^{37}Cl$) and right panel ($H^{35}Cl$). The overall accuracies in these plots are the root sum squares (RSS) of the precision and the estimated systematic error due to systematic effects of the two particular profiles. The precision for TELIS is ≈0.01 ppbv, the TELIS systematic error estimate is 0.05–0.4 ppbv, the MLS precision 0.15–0.4 ppbv, and the systematic error in MLS is taken constant as 0.1 ppbv (Froidevaux et al., 2008). Within these margins, the HCl profiles by TELIS and MLS agree over almost the entire altitude range of 10–35 km. The two TELIS profiles are consistent above 20 km. Only at 24 km the difference exceeds the error margin with ≈0.1 ppbv. Also between 15 and 20 km the difference falls outside the error margin. The differences between TELIS and MLS are only around 22 km ($H^{37}Cl$) and 25 km ($H^{35}Cl$), a few times 0.01 ppbv beyond the uncertainty boundaries. One reason why all profiles fall so well within the uncertainty boundaries could be that the depicted uncertainty is the root sum square of all systematic effects. In the differences, however, it might be that certain errors cancel; for instance spectroscopic errors. On the other hand, it may also suggest that some systematic errors are being overestimated.

In Fig. 6 the decomposition of the TELIS systematic errors for the HCl retrievals are shown. Several error sources have been grouped together. The spectroscopy error is due to uncertainties in the spectroscopic widths and line strengths of

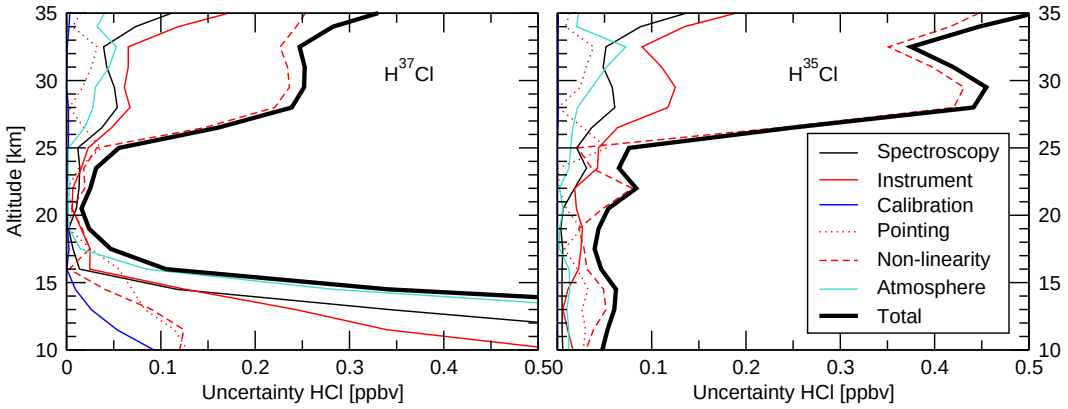

Fig. 6. The individual estimates of systematic effects in the HCl profiles based on the $H^{37}Cl$ line (left panel) and the $H^{35}Cl$ line (right panel). Several systematic error sources have been grouped together. In black the spectroscopic error is given for uncertainties in the spectral widths and line strengths of the HCl lines. In red the errors of various instrumental uncertainties are shown; the solid red line combines the errors due to uncertainties in field of view, local oscillator frequency, instrumental line shape, and sideband ratio, the dotted red line refers to the absolute pointing, and the dashed red line to the non-linearity of the detector response function. In blue the systematic error due to the radiometric calibration is given and in turquoise the systematic error by uncertainties in the atmospheric condition (temperature and pressure profiles). The thick black line is the RSS of these errors.

the HCl lines. The instrumental error combines the error due to uncertainties in the field of view, the local oscillator frequency, the instrumental line shape, and the sideband ratio. The pointing error is due to the uncertainty in the absolute viewing geometry. In many limb studies this error is of deciding importance and is therefore mentioned separately and is not included in the instrumental error. Also, the systematic error by the non-linearity is not included in the instrumental error. The calibration error is due to the uncertainty in the temperature of the on-board reference black body. Finally, the atmospheric error is a composite of uncertainties in the temperature and pressure profiles.

As explained in Sect. 2.1, the uncertainty in the non-linearity of the detector's response function is large. This is also reflected in its contribution to the total error budget. Above 25 km, it is clearly the dominant error source (0.05–0.4 ppbv) for both isotopes. In the case of $H^{35}Cl$ this error is dominant below 25 km as well, but in this range the contribution is on the order of 0.05 ppbv. For $H^{37}Cl$, various error sources, including the error by the non-linearity, are comparable between 17 and 25 km (each 0.01–0.02 ppbv). From the left panel of Fig. 1, it can be seen that the $H^{35}Cl$ line is stronger than the $H^{37}Cl$ line. As the non-linearity has the heighest impact on retrievals with strong lines, this explains why this error source is larger for $H^{35}Cl$ than for $H^{37}Cl$ in this altitude range. Below 17 km, however, all errors steeply increase for $H^{37}Cl$, surpassing those of $H^{35}Cl$.

In Fig. 5 the difference profiles for $H^{37}Cl$ (left and centre) panel, show a similar shape. From these plots it may be concluded that the HCl abundance is underestimated in case of $H^{37}Cl$ retrieval. One reason could be that the compression of 17.5 %, due to the non-linearity, is overestimated for this particular retrieval. The higher the non-linearity parameter, the more signal compression will occur. The highest compression will occur for the measurement with the highest total power, i.e. the hot calibration measurement. Bearing lower total power, the compression for the atmospheric signal will be lower than for this calibration measurement. In the calibrated spectra this will result in stronger spectral lines, which in turn leads to an overestimation in the retrieved profiles when the non-linearity is not accounted for. When the non-linearity is taken into account in the retrievals, the retrieved profiles will show lower concentration levels with an increasing non-linearity parameter. Therefore, an overestimation of the non-linearity parameter will result in an underestimation of the retrieved profile.

The next largest systematic error is due to instrumental uncertainties. Of the four combined error sources, the sideband ratio is the main uncertainty. Also, this error is significantly higher in the altitude range of 25–35 km than between 17 and 25 km, indicating that this systematic error increases with HCl concentrations. This can be understood as the sidebands scale with the sideband ratio and an error in this ratio results in a scaling error of the spectral features and thus in retrieved concentrations. In case of $H^{37}Cl$ the error is <0.1 ppbv down to 15 km. In the case of $H^{35}Cl$, however, this error exceeds the 0.1 ppbv level above 28 km.

For both isotopes the spectroscopic error is the third largest contribution to the error budget at altitudes above 25 km, which corresponds to the altitude range with nominal HCl abundances. As this error increases with the line strength and thus with the HCl concentration, the contribution of this error is negligible below 25 km where the chlorine reservoir species have been converted into active chlorine. Below 17 km, the abundances are nominal as well, but are low (<1 ppbv) and here this error is not prevalent either.

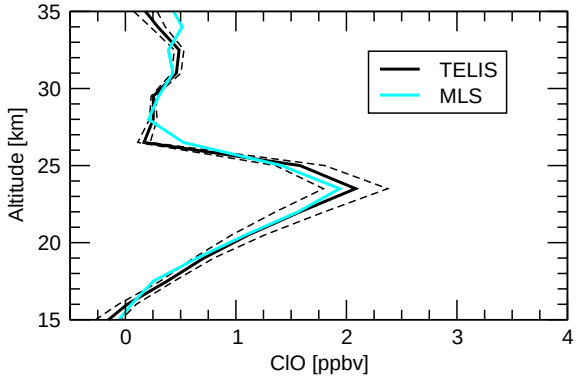

Fig. 7. The retrieved ClO vertical profile in ppbv from the TELIS balloon flight on 24 January 2010 in chlorine activated Arctic air. ClO is a member of the active chlorine chemical family and the peak in the profile around 23 km is because of the conversion of inactive reservoir chlorine into active chlorine. The retrieved profile by TELIS is given in black and the dashed lines refer to the estimated overall accuracy of this profile. The profile by the MLS satellite instrument is given in blue.

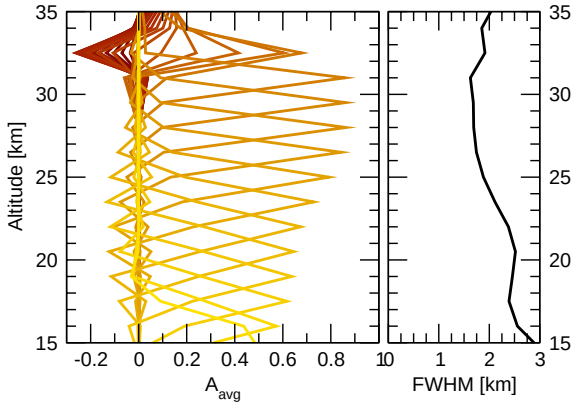

Fig. 8. On the left the averaging kernel for ClO is depicted with the corresponding FWHM on the right.

The remaining systematic errors, due to uncertainties in calibration, pointing and atmospheric parameters, are relatively small. Although in many studies the uncertainty in the pointing appears as a major contributor to the total error budget for limb retrievals, this is not so much the case here, thanks to the high-performance MIPAS attitude and reference system (Friedl-Vallon et al., 2004). For both HCl isotopes the uncertainty is well below 0.05 ppbv over almost the whole altitude range. For $H^{37}Cl$, the systematic error by atmospheric uncertainties is below 0.05 ppbv for altitudes above 17 km. In case of $H^{35}Cl$, the contribution is below 0.05 ppbv over the whole altitude range, except at 32.5 km (0.07 ppbv), being the highest tangent height in the limb recordings. Finally, the calibration error is so small that it is only discernible in Fig. 6 for the lowest altitudes and is thus of no concern.

The overall accuracy is taken as the root sum square of all contributions mentioned above, rather than a direct sum, treating the systematic errors as quasi-statistical. In Fig. 6 the total accuracy is indicated by the thick black line. For $H^{37}Cl$ this total increases from 20 km to 35 km from 0.02 ppbv to 0.3 ppbv. The main contribution is due to the uncertainty in the non-linearity of the detector. Below 20 km the total accuracy increases, first slowly, but then beyond 17 km steeply to more than 1 ppbv at 10 km and reflects the saturation of the HCl line at these altitudes. For $H^{35}Cl$ the increase is slowly from 0.05 ppbv at 10 km to 0.09 ppbv at 25 km. Above 25 km the air becomes non-activated, leading to a steep HCl gradient as function of altitude. The corresponding total error increases rapidly in this altitude range as well to ≈0.45 ppbv at 28 km.

4.2 ClO retrieval

During the investigated balloon flight, ClO has been measured for 1.5 h to monitor its increase during sunrise with a 1 min temporal resolution corresponding to the recording time of a single limb scan.

ClO profile retrievals have been performed for every single limb sequence and a profile during daytime equilibrium is depicted in Fig. 7 by the solid black line. The two dashed lines indicate the uncertainty in the ClO profile. The ClO concentration peaks around 23 km to 2.1 ppbv, indicating that the air was highly chlorine activated. The ClO profile by the MLS satellite instrument is plotted in blue.

The averaging kernel is shown in the left panel of Fig. 8. In the right panel the FWHM of the averaging kernel is shown. Up to the highest tangent height (32.5 km), the kernel is nicely peaked with a FWHM of 2–2.5 km in the altitude range with activated air (17–26 km), which is very comparable to the widths in case of the HCl retrievals.

As with the HCl retrievals, the retrieval noise is only 0.01 ppbv because of the very low measurement noise. The overall accuracy in the TELIS ClO profile is thus almost entirely determined by systematic effects due to limited knowledge of atmospheric and instrumental parameters. The contributions to the total systematic error by various sources are plotted in Fig. 9. Here, several errors have been grouped together in the same way as in Fig. 6. Analogous to HCl, the largest uncertainty stems from the non-linear behaviour of the detector (0.24 ppbv). Of the remaining uncertainties, the limited accuracies in the spectroscopic database (0.14 ppbv), the uncertainty in the absolute pointing (0.06 ppbv) and in the sideband ratio (included in the instrument error; 0.05 ppbv) are the largest contributors to the total error budget. This is significantly more than the total systematic error in the MLS ClO profiles, which has been estimated to be better than 0.04 ppbv (Santee et al., 2008). Even without taking the large uncertainty in the non-linearity into account, the

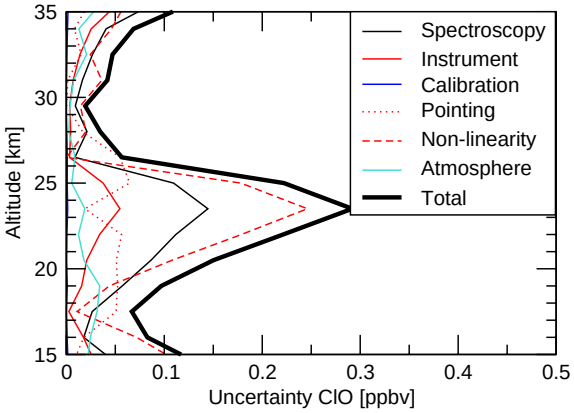

Fig. 9. The individual estimates of systematic effects in the ClO profile. Several systematic error sources have been grouped together. In black the spectroscopic error is given for uncertainties in the spectral widths and line strengths of the HCl lines. In red the systematic errors due to various instrumental uncertainties are shown; the solid red line combines the systematic errors due to uncertainties in field of view, local oscillator frequency, instrumental line shape, and sideband ratio, the dotted red line refers to the absolute pointing, and the dashed red line to the non-linearity of the detector response function. In blue the systematic error due to the radiometric calibration is given and in turquoise the systematic error by uncertainties in the atmospheric condition (temperature and pressure profiles). The thick black line is the RSS of these errors.

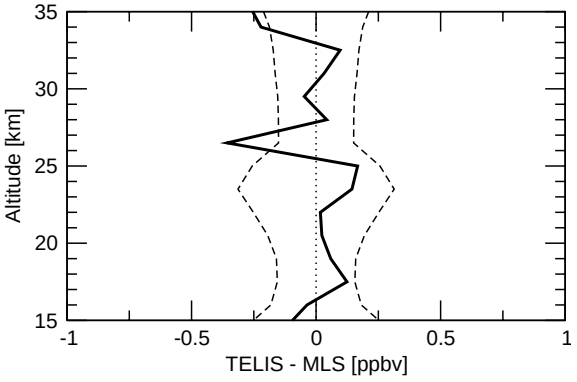

Fig. 10. The difference between the TELIS and MLS ClO profiles is plotted (solid line). The dashed lines indicate the RSS of the retrieval errors and the estimated systematic effects of both TELIS and MLS.

total accuracy for the TELIS ClO profiles is still 0.15 ppbv at the ClO peak. A striking difference in the error budgets of the TELIS and MLS instruments is the contribution of the spectroscopy uncertainties. This error source is the second largest for TELIS but is minor in the MLS ClO error budget (<0.01 ppbv) (Santee et al., 2008). One explanation may be that this error scales with ClO abundances and in case of TELIS this error refers to measurements in activated air with a ten-fold higher than nominal ClO concentration levels. This is not only true for the spectroscopic error, but also other systematic errors, e.g. the sideband ratio error, may depend on spectral line strengths and thus ClO concentrations. Another explanation may be that the cited uncertainties in the HITRAN 2008 database are overestimated. This is supported by the fact that the permanent electric dipole moment for ClO is known within 0.2 % (Yaron et al., 1988), which is much better than the cited line strength uncertainty of 5 % in the HITRAN database. It is noted, however, that apart from the error in the electric dipole moment, the temperature error propagates into the line strength error as well due to temperature dependancy of the Boltzmann distribution in level population. Nevertheless, the 5 % error estimate seems to be on the conservative side.

In Fig. 10 the difference between the TELIS and MLS ClO profiles is plotted for daytime equilibrium conditions. The dashed lines correspond to the root sum square of the TELIS retrieval error (less than 0.01 ppbv), estimated systematic errors due to limited knowledge of instrumental and atmospheric parameters for TELIS (0.05–0.3 ppbv), the MLS retrieval error (≈0.15 ppbv), and the MLS systematic errors (0.01–0.04 ppbv) (Santee et al., 2008). Within these uncertainties the two profiles correspond to each other over almost the entire altitude range. Only at 26.5 km does the difference exceed the uncertainty boundaries. As with HCl, the overall agreement might indicate that errors cancel when differences are determined, or that the error margin is overestimated.

For the altitude range 17.5–23.5 km, the temporal variation of ClO is depicted in Fig. 11. The temporal resolution is 1 min, corresponding to the recording time of a single limb sequence. The data gaps are due to additional calibration measurements. During the measurements the azimuth of the limb path was taken perpendicular to the rising sun to ensure uniform illumination of the line of sight. The ClO concentration clearly increases for all altitudes after 07:40 UTC. It is noted that the onset of this increase is slightly earlier for higher altitudes which is a geometric effect as the sun appears first over the horizon at these altitudes. The sunrise at these altitudes is between 06:58 UTC (23.5 km) and 07:05 UTC (17.5 km) for the geo-locations during this particular flight. The increase of daytime ClO concentration levels starts thus ≈40 min after the local sunrise. This lag may be caused by clouds blocking the solar radiation when the sun is still very low over the horizon.

5 Conclusions

For the first time, profile retrievals have been demonstrated for the balloon instrument TELIS. The balloon flight took place in chlorine activated Arctic air conditions in 2010 and both active chlorine (ClO) and inactive chlorine (HCl) have been recorded.

Two HCl profiles, derived from two different isotopes, are presented and are internally consistent. Both are successfully

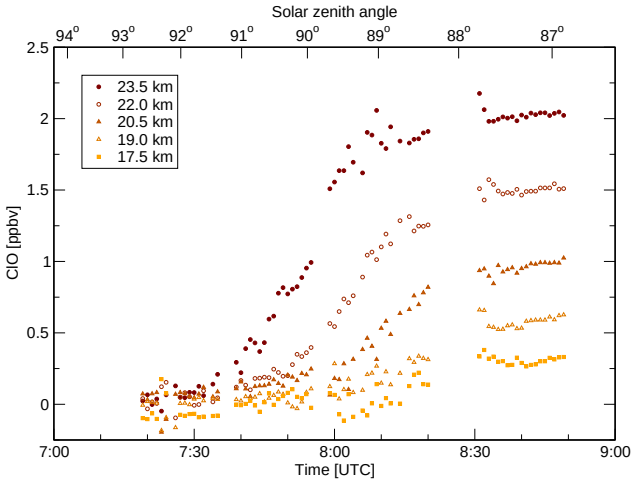

Fig. 11. The ClO concentration as function of time for five different altitudes in the range 17.5–23.5 km. The temporal resolution is 1 min. The data gaps are due to additional calibration measurements. The onset of the increase in ClO starts first for higher altitudes because the sunrise occurs earlier at these altitudes.

validated against the HCl profile by the MLS satellite instrument. The differences fall well within the uncertainties. Because of the low measurement noise, the precision in the HCl retrievals is better than 0.01 ppbv and the overall accuracy is almost fully determined by systematic effects. This overall accuracy is 0.05–0.4 ppbv and stems mostly from the largely unknown non-linear response function of the detector. Over the altitude range 15–35 km, the FWHM of the averaging kernel is for TELIS 1.8–2.9 km ($H^{35}Cl$). This is close to the field of view (1.5 km) and the vertical sampling between two consecutive tangent heights (also 1.5 km). ClO shows a daily cycle in concentration and its increase from nighttime to daytime levels has been monitored with a 1 min temporal resolution. A profile, determined from a limb sequence recorded under daytime equilibrium conditions, is successfully validated against the MLS daytime ClO profile. The TELIS precision is less than 0.01 ppbv because of the low measurement noise and the overall accuracy in the ClO profile is, analogous to the HCl retrievals, fully determined by systematic effects. The accuracy is maximal 0.3 ppbv for the peak in the profile during daytime equilibrium and the main contributor is the uncertainty in the non-linear response function of the detector. The FWHM of the averaging kernel is 2.0–2.5 km in the altitude range with chlorine activated air (17–26 km). Because the HCl and ClO retrieval accuracy is dominated by systematic errors, the retrieval performance can be improved by a better characterisation of the instrument. In this context, the reduction of the non-linearity uncertainty of the TELIS instrument is a topic of on-going research. However, this is non-trivial, as relevant electronic components are deeply embedded within the spectrometer. Furthermore, a consolidation and improvement of the sideband ratios are planned.

In addition, cross-validations will be performed with the ISS/SMILES, Odin/SMR, and ACE/FTS instruments. In particular, the SMILES and SMR instruments are interesting since they observe exactly the same transitions of HCl (SMILES) and ClO (SMR).

In the future, TELIS profiles of HCl and ClO will be complemented by HOCl, and together with the MIPAS profiles of chlorine species ($ClONO_2$ and the ClO-dimer), these form an extended set of active and inactive chlorine species. This set will be used to test and constrain atmospheric chemistry models. The retrieved ClO profiles from TELIS and MIPAS data, thus pertaining to different sensors in different spectral ranges, will also be used for cross-comparison purposes. As the flight took place in chlorine activated air, the increase of ClO levels during sunrise originates mostly from photodissociation of the ClO-dimer. The presented time series of the ClO profiles will be used to investigate the rates of this dissociation under atmospheric pressure and temperature conditions.

Acknowledgements. The authors would like to acknowledge H. Golstein, P. Yagoubov, N. Suttiwong, H. Nordmeyer, Ch. Satorius, and A. Kleinert, for their contributions to the TELIS project. G. Wetzel is thanked for sharing the retrieved atmospheric profiles by the MIPAS instrument. The authors would also like to acknowledge the employees of the SSC Esrange facility, who showed a positive attitude and a willingness to adapt schedules to enable the balloon flight with the highest prospects. The balloon launch was co-funded by the German Space Agency, DLR-MORABA, and SRON.

Edited by: H. Worden

References

Anderson, G., Chetwynd, J., Clough, S., Shettle, E., and Kneizys, F.: AFGL atmospheric constituent profiles (0–120 km), Tech. Rep. AFGL-TR-86-0110, Air Force Geophysics Laboratory, Hanscom Air Force Base, Bedford, Mass., 1986.

Austin, J., Scinocca, J., Plummer, D., Oman, L., Waugh, D., Akiyoshi, H., Bekki, S., Braesicke, P., Butchart, N., Chipperfield, M., Cugnet, D., Dameris, M., Dhomse, S., Eyring, V., Frith, S., Garcia, R., Garny, H., Gettelman, A., Hardiman, S., Kinnison, D., Lamarque, J., Mancini, E., Marchand, M., Michou, M., Morgenstern, O., Nakamura, T., Pawson, S., Pitari, G., Pyle, J., Rozanov, E., Shepherd, T., Shibata, K., Teyssedre, H., Wilson, R., and Yamashita, Y.: Decline and recovery of total column ozone using a multimodel time series analysis, J. Geophys. Res., 115, D00M10, doi:10.1029/2010JD013857, 2010.

Barath, F., Chavez, M., Cofield, R., Flower, D., Frerking, M., Gram, M., Harris, W., Holden, J., Jarnot, R., Kloezeman, W., Klose, G., Lau, G., Loo, M., Maddison, B., Mattauch, R., McKinney, R., Peckham, G., Pickett, H., Siebes, G., Soltis, F., Suttie, R., Tarsala, J., Waters, J., and Wilson, W.: The Upper-Atmosphere Research Satellite Microwave Limb Sounder instrument, J. Geophys. Res., 98, 10751–10762, doi:10.1029/93JD00798, 1993.

Bernath, P., McElroy, C., Abrams, M., Boone, C., Butler, M., Camy-Peyret, C., Carleer, M., Clerbaux, C., Coheur, P.-F., Colin, R., DeCola, P., DeMazière, M., Drummond, J., Dufour, D., Evans, W., Fast, H., Fussen, D., Gilbert, K., Jennings, D., Llewellyn, E., Lowe, R., Mahieu, E., McConnell, J., McHugh, M., McLeod, S., Michaud, R., Midwinter, C., Nassar, R., Nichitiu, F., Nowlan, C., Rinsland, C., Rochon, Y., Rowlands, N., Semeniuk, K., Simon, P., Skelton, R., Sloan, J., Soucy, M.-A., Strong, K., Tremblay, P., Turnbull, D., Walker, K., Walkty, I., Wardle, D., Wehrle, V., Zander, R., and Zou, J.: Atmospheric Chemistry Experiment (ACE): Mission overview, Geophys. Res. Lett., 32, L15S01, doi:10.1029/2005GL022386, 2005.

Birk, M. and Wagner, G.: Results of antenna beam profile measurements August 2009, Tech. Rep. TELIS-DLR-ANTBEAM, Deutsches Zentrum für Luft und Raumfahrt, Wessling, Germany, 2009.

Birk, M., Wagner, G., de Lange, G., de Lange, A., Ellison, B., Harman, M., Murk, A., Oelhaf, H., Maucher, G., and Sartorius, C.: TELIS: TErahertz ans subMMW LImb Sounder – Project Summary After First Successful Flight, in: Proceedings of the 21st International Symposium on Space Terahertz Technology, University of Oxford and STFC Rutherford Appleton Laboratory, Oxford, UK, 195–202, 2010.

Buehler, S., Eriksson, P., Kuhn, T., von Engeln, A., and Verdesa, C.: ARTS, the atmospheric radiative transfer simulator, J. Quant. Spectrosc. Ra., 91, 65–93, doi:10.1016/j.jqsrt.2004.05.051, 2005.

de Lange, A., Landgraf, J., and Hoogeveen, R.: Stratospheric isotopic water profiles from a single submillimeter limb scan by TELIS, Atmos. Meas. Tech., 2, 423–435, doi:10.5194/amt-2-423-2009, 2009.

de Lange, G., Birk, M., Boersma, D., Dercksen, J., Dmitriev, P., Ermakov, A., Filippenko, L., Golstein, H., Hoogeveen, R., de Jong, L., Khudchenko, A., Kinev, N., Kiselev, O., van Kuik, B., de Lange, A., van Rantwijk, J., Selig, A., Sobolev, A., Torgashin, M., de Vries, E., Wagner, G., Yagoubov, P., and Koshelets, V.: Development and characterization of the superconducting integrated receiver channel of the TELIS atmospheric sounder, Supercond. Sci. Technol., 23, 045016, doi:10.1088/0953-2048/23/4/045016, 2010.

Eldén: Algorithms for regularization of ill-conditioned least-squares problems, Bit, 17, 134–145, 1977.

Friedl-Vallon, F., Maucher, G., Seefeldner, M., Trieschmann, O., Kleinert, A., Lengel, A., Keim, C., Oelhaf, H., and Fischer, H.: Design and characterization of the balloon-borne michelson interferometer for passive atmospheric sounding (MIPAS-B2), Appl. Optics, 43, 3335–3355, 2004.

Frisk, U., Hagström, M., Ala-Laurinaho, J., Andersson, S., Berges, J.-C., Chabaud, J.-P., Dahlgren, M., Emrich, A., Florén, H.-G., Florin, G., Fredrixon, M., Gaier, T., Haas, R., Hirvonen, T., Hjalmarsson, Å., Jakobsson, B., Jukkala, P., Kildal, P., Kollberg, E., Lassing, J., Lecacheux, A., Lehikoinen, P., Lehto, A., Mallat, J., Marty, C., Michet, D., Narbonne, J., Nexon, M., Olberg, M., Olofsson, A. O. H., Olofsson, G., Origné, A., Petersson, M., Piironen, P., Pons, R., Pouliquen, D., Ristorcelli, I., Rosolen, C., Rouaix, G., Räisänen, A. V., Serra, G., Sjöberg, F., Stenmark, L., Torchinsky, S., Tuovinen, J., Ullberg, C., Vinterhav, E., Wadefalk, N., Zirath, H., Zimmermann, P., and Zimmermann, R.: The Odin satellite – I. Radiometer design and test, Astron. Astrophys., 402, L27–L34, doi:10.1051/0004-6361:20030335, 2003.

Froidevaux, L., Jiang, Y., Lambert, A., Livesey, N., Read, W., Waters, J., Fuller, R., Marcy, T., Popp, P., Gao, R., Fahey, D., Jucks, K., Stachnik, R., Toon, G., Christensen, L., Webster, C., Bernath, P., Boone, C., Walker, K., Pumphrey, H., Harwood, R., Manney, G., Schwartz, M., Daffer, W., Drouin, B., Cofield, R., Cuddy, D., Jarnot, R., Knosp, B., Perun, V., Snyder, W., Stek, P., Thurstans, R., and Wagner, P.: Validation of Aura Microwave Limb Sounder HCl measurements, J. Geophys. Res., 113, D15S25, doi:10.1029/2007JD009025, 2008.

Glatthor, N., von Clarmann, T., Fischer, H., Grabowski, U., Hopfner, M., Kellmann, S., Kiefer, M., Linden, A., Milz, M., Steck, T., Stiller, G., Tsidu, G., Wang, D., and Funke, B.: Spaceborne ClO observations by the Michelson Interferometer for Passive Atmospheric Sounding (MIPAS) before and during the antarctic major warming in September/October 2002, J. Geophys. Res., 109, D11307, doi:10.1029/2003JD004440, 2004.

Hansen, P.: Analysis of discrete ill posed problems by means of the L-curve, SIAM Rev., 34, 561–580, 1992.

Irimajiri, Y., Manabe, T., Ochiai, S., Masuko, H., Yamagami, T., Saito, Y., Izutsu, N., Kawasaki, T., Namiki, M., and Murata, I.: BSMILES – A balloon-borne superconducting submillimeter-wave limb-emission sounder for stratospheric measurements, IEEE T. Geosci. Remote Sens. Lett., 3, 88–92, doi:10.1109/LGRS.2005.856712, 2006.

Jin, B., Chen, I., Huang, W., Lien, C., Guchhait, N., and Lin, J.: Photodissociation Cross Section of ClOOCl at 330 nm, J. Phys. Chem. A, 114, 4791–4797, doi:10.1021/jp909374k, 2010.

Jones, A., Urban, J., Murtagh, D. P., Sanchez, C., Walker, K. A., Livesey, N. J., Froidevaux, L., and Santee, M. L.: Analysis of HCl and ClO time series in the upper stratosphere using satellite data sets, Atmos. Chem. Phys., 11, 5321–5333, doi:10.5194/acp-11-5321-2011, 2011.

Kikuchi, K., Nishibori, T., Ochiai, S., Ozeki, H., Irimajiri, Y., Kasai, Y., Koike, M., Manabe, T., Mizukoshi, K., Murayama, Y., Nagahama, T., Sano, T., Sato, R., Seta, M., Takahashi, C., Takayanagi, M., Masuko, H., Inatani, J., Suzuki, M., and Shiotani, M.: Overview and early results of the Superconducting Submillimeter-Wave Limb-Emission Sounder (SMILES), J. Geophys. Res., 115, D23306, doi:10.1029/2010JD014379, 2010.

Kulkarni, S. and Heiles, C.: How to obtain the true correlation from a 3-level digital correlator, Astron. J., 85, 1413–1420, 1980.

Liebe, H., Hufford, G., and Cotton, M.: Propagation modeling of moist air and suspended water/ice particles at frequencies below 1000 GHz, Proc. NATO/AGARD Wave Propagation Panel, 52nd meeting, 1993.

Lien, C., Lin, W., Chen, H., Huang, W., Jin, B., Chen, I., and Lin, J.: Photodissociation cross sections of ClOOCl at 248.4 and 266 nm, J. Chem. Phys., 131, 174301, doi:10.1063/1.3257682, 2009.

Moreau, G., Robert, C., Catoire, V., Chartier, M., Camy-Peyret, C., Huret, N., Pirre, M., Pomathiod, L., and Chalumeau, G.: SPIRALE: a multispecies in situ balloonborne instrument with six tunable diode laser spectrometers, Appl. Optics, 44, 5972–5989, doi:10.1364/AO.44.005972, 2005.

Ochiai, S., Kikuchi, K., Nishibori, T., Manabe, T., Ozeki, H., Sato, R., Sano, T., Irimajiri, Y., and Shiotani, M.: In-orbit performance and calibration of SMILES, in: 35th International Conference on Infrared, Millimeter, and Terahertz Waves

(IRMMW-THZ 2010), p.WOS:000288130600459, IEEE, Rome, Italy, 2010.

Papanastasiou, D., Papadimitriou, V., Fahey, D., and Burkholder, J.: UV Absorption Spectrum of the ClO Dimer (Cl(2)O(2)) between 200 and 420 nm, J. Phys. Chem. A, 113, 13711–13726, doi:10.1021/jp9065345, 2009.

Phillips, P.: A technique for the numerical solution of certain integral equations of the first kind, J. Assoc. Comput. Mach., 9, 84–97, 1962.

Pope, F., Hansen, J., Bayes, K., Friedl, R., and Sander, S.: Ultraviolet absorption spectrum of chlorine peroxide ClOOCl, J. Phys. Chem. A, 111, 4322–4332, 2007.

Rothman, L., Gordon, I., Barbe, A., Benner, D. C., Bernath, P., Birk, M., Boudon, V., Brown, L., Campargue, A., Champion, J.-P., Chance, K., Coudert, L., Dana, V., Devi, V., Fally, S., Flaud, J.-M., Gamache, R., Goldman, A., Jacquemart, D., Kleiner, I., Lacome, N., Lafferty, W., Mandin, J.-Y., Massie, S., Mikhailenko, S., Miller, C., Moazzen-Ahmadi, N., Naumenko, O., Nikitin, A., Orphal, J., Perevalov, V., Perrin, A., Predoi-Cross, A., Rinsland, C., Rotger, M., Šimečková, M., Smith, M., Sung, K., Tashkun, S., Tennyson, J., Toth, R., Vandaele, A., and Auwera, J. V.: The HITRAN 2008 molecular spectroscopic database, J. Quant. Spectrosc. Ra., 110, 533–572, doi:10.1016/j.jqsrt.2009.02.013, 2009.

Russell, J., Gordley, L., Park, J., Drayson, S., Hesketh, W., Cicerone, R., Tuck, A., Frederick, J., Harries, J., and Crutzen, P.: The Halogen Occultation Experiment, J. Geophys. Res., 98, 10777–10797, 1993.

Santee, M., Lambert, A., Read, W., Livesey, N., Manney, G., Cofield, R., Cuddy, D., Daffer, W., Drouin, B., Froidevaux, L., Fuller, R., Jarnot, R., Knosp, B., Perun, V., Snyder, W., Stek, P., Thurstans, R., Wagner, P., Waters, J., Connor, B., Urban, J., Murtagh, D., Ricaud, P., Barrett, B., Kleinboehl, A., Kuttippurath, J., Kullmann, H., von Hobe, M., Toon, G., and Stachnik, R.: Validation of the Aura Microwave Limb Sounder ClO Measurements, J. Geophys. Res., 113, D15S22, doi:10.1029/2007JD008762, 2008.

Schimpf, B. and Schreier, F.: Robust and efficient inversion of vertical sounding atmospheric high-resolution spectra by means of regularization, J. Geophys. Res., 102, 16037–16055, doi:10.1029/97JD00847, 1997.

Solomon, S.: Stratospheric ozone depletion: a review of concepts and history, Rev. Geophys., 37, 275–316, 1999.

Steck, T.: Methods for determining regularization for atmospheric retrieval problems, Appl. Optics, 41, 1788–1797, 2002.

Tikhonov, A.: On the solution of incorrectly stated problems and a method of regularization, Dokl. Akad. Nauk SSSR, 151, 501–504, 1963.

Twomey, S.: On the numerical solution of Fredholm integral equations of the first kind by inversion of the linear system produced by quadrature, J. Assoc. Comput. Mach., 10, 97–101, 1963.

von Hobe, M., Salawitch, R. J., Canty, T., Keller-Rudek, H., Moortgat, G. K., Grooß, J.-U., Müller, R., and Stroh, F.: Understanding the kinetics of the ClO dimer cycle, Atmos. Chem. Phys., 7, 3055–3069, doi:10.5194/acp-7-3055-2007, 2007.

von Hobe, M., Stroh, F., Beckers, H., Benter, T., and Willner, H.: The UV/Vis absorption spectrum of matrix-isolated dichlorine peroxide, ClOOCl, Phys. Chem. Chem. Phys., 11, 1571–1580, doi:10.1039/b814373k, 2009.

Waters, J., Froidevaux, L., Harwood, R., Jarnot, R., Pickett, H., Read, W., Siegel, P., Cofield, R., Filipiak, M., Flower, D., Holden, J., Lau, G., Livesey, N., Manney, G., Pumphrey, H., Santee, M., Wu, D., Cuddy, D., Lay, R., Loo, M., Perun, V., Schwartz, M., Stek, P., Thurstans, R., Boyles, M., Chandra, K., Chavez, M., Chen, G., Chudasama, B., Dodge, R., Fuller, R., Girard, M., Jiang, J., Jiang, Y., Knosp, B., LaBelle, R., Lam, J., Lee, K., Miller, D., Oswald, J., Patel, N., Pukala, D., Quintero, O., Scaff, D., Snyder, W. V., Tope, M., Wagner, P., and Walch, M.: The Earth Observing System Microwave Limb Sounder (EOS MLS) on the Aura satellite, IEEE T. Geosci. Remote, 44, 1075–1092, doi:10.1109/TGRS.2006.873771, 2006.

Webster, C., May, R., Jaeglé, L., Hu, H., Sander, S., Gunson, M., Toon, G., Russell III, J. R., Stimpfle, R., Koplow, J., Salawitch, R., and Michelsen, H.: Hydrochloric acid and the chlorine budget of the lower stratosphere, Geophys. Res. Lett., 21, 2575–2578, 1994.

Weidner, F., Bösch, H., Bovensmann, H., Burrows, J. P., Butz, A., Camy-Peyret, C., Dorf, M., Gerilowski, K., Gurlit, W., Platt, U., von Friedeburg, C., Wagner, T., and Pfeilsticker, K.: Balloon-borne limb profiling of UV/vis skylight radiances, O_3, NO_2, and BrO: technical set-up and validation of the method, Atmos. Chem. Phys., 5, 1409–1422, doi:10.5194/acp-5-1409-2005, 2005.

Wetzel, G., Oelhaf, H., Ruhnke, R., Friedl-Vallon, F., Kleinert, A., Kouker, W., Maucher, G., Reddmann, T., Seefeldner, M., Stowasser, M., Trieschmann, O., von Clarmann, T., and Fischer, H.: NOy partitioning and budget and its correlation with N_2O in the Arctic vortex and in summer mid-latitudes in 1997, J. Geophys. Res., 107, 4280, doi:10.1029/2001JD000916, 2002.

Wetzel, G., Oelhaf, H., Kirner, O., Ruhnke, R., Friedl-Vallon, F., Kleinert, A., Maucher, G., Fischer, H., Birk, M., Wagner, G., and Engel, A.: First remote sensing measurements of ClOOCl along with ClO and $ClONO_2$ in activated and deactivated Arctic vortex conditions using new ClOOCl IR absorption cross sections, Atmos. Chem. Phys., 10, 931–945, doi:10.5194/acp-10-931-2010, 2010.

Yaron, D., Peterson, K., and Klemperer, W.: On the Dipole Moment Functions of ClO and OH, J. Chem. Phys., 88, 4702–4710, 1988.